Heliyon 10 (2024) e30817

Contents lists available at ScienceDirect

Heliyon

journal homepage: www.cell.com/heliyon

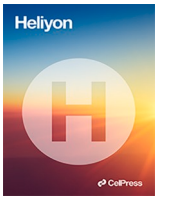

Research article

Synergistic adsorption and photocatalysis study of TiO_2 and activated carbon composite

Yihang Yue [a,1], Xiaoju Yue [a,b,1], Xiaofeng Tang [c,**], Lin Han [a,b], Jinnong Wang [a,b], Shifeng Wang [a,d,e,*], Chun Du [a,***]

[a] Key Laboratory of Plateau Oxygen and Living Environment of Tibet Autonomous Region, College of Science, Tibet University, Lhasa 850000, China
[b] Hoffmann Institute of Advanced Materials, Shenzhen Polytechnic University, Shenzhen, 518055, China
[c] Tibet Museum of Natural Science, Lhasa, 850000, China
[d] Fujian Quanzhou Peninsula Materials Co., Ltd, Quanzhou, 362000, China
[e] Aimoli (Hebei) Technology Co., Ltd, Shijiazhuang, 050000, China

ARTICLE INFO

Keywords:
Synergistic degradation
Titanium dioxide
Highland barley straw
Activated carbon

ABSTRACT

The discharge of organic pollutants by the textile and dyeing industries presents an escalating threat to aquatic environments, necessitating the development of effective remediation strategies. This study introduces the utilization of graphite-like structured activated carbon (AC), derived from highland barley straw—a biomass unique to the Plateau regions of China, including Tibet, Qinghai, and Gansu—as a support material for the TiO_2 catalyst. TiO_2/AC composites with different TiO_2 loadings were synthesized by ultrasonic impregnation. The TiO_2/AC composites were found to be polycrystalline materials composed of anatase and rutile phases. The TiO_2 nanoparticles are well-dispersed over the surface of the AC. The photocatalytic activity of these composites was evaluated through their capacity to degrade a methylene blue (MB) solution upon irradiation. It was observed that the inclusion of TiO_2 increases the number of adsorption sites and active sites for methylene blue, with the photocatalytic activity being notably higher at a 3-wt % TiO_2 loading, achieving a remarkable 99.6 % degradation efficiency for 100 mg/L MB within 100 min. The experimental kinetic data for the photocatalytic process follow the pseudo-first-order kinetic model. Furthermore, TiO_2/AC retains high photocatalytic activity after five reaction cycles. This research provides valuable insights into the application of biomass-derived materials for the purification of water, offering a sustainable solution to both pollution and agricultural waste challenges in Plateau areas of China.

1. Introduction

Recent studies have shown that industrial development has had an increasingly negative impact on the environment. In particular,

* Corresponding author. Tibet Key Laboratory of Plateau Oxygen and Living Environment, College of Science, Tibet University, Lhasa 850000, PR China.
** Corresponding author.
*** Corresponding author.
E-mail addresses: yueyh1997@163.com (Y. Yue), yuexiaoju@utibet.edu.cn (X. Yue), tangxiaofengtm@163.com (X. Tang), hanlin@utibet.edu.cn (L. Han), wangjinnong@utibet.edu.cn (J. Wang), wsf@utibet.edu.cn (S. Wang), duchun@utibet.edu.cn (C. Du).
[1] These authors contributed equally to this work.

https://doi.org/10.1016/j.heliyon.2024.e30817
Received 28 October 2023; Received in revised form 17 April 2024; Accepted 6 May 2024
Available online 7 May 2024

the industrial production of organic pollutants such as pesticides, dyes, and antibiotics poses a threat to both the environment and living organisms, thereby impeding the sustainable and healthy development of human society [1,2]. China is a major producer of dyestuffs, with the chemical dyestuffs industry ranking first globally in terms of scale. According to statistics from the China Dyestuff Association, the average annual output of Chinese dyestuffs has reached an impressive 807,800 tons during the five years from 2018 to 2022, with an estimated output of 904,000 tons in 2023. According to reliable data, the textile printing and dyeing industry accounts for 7.5 % of the national industrial wastewater discharge statistics, ranking fifth in terms of total wastewater discharge within the national industrial sector, with an annual total of 1.413 billion tons. Consequently, it significantly contributes to environmental pollution. However, water scarcity currently affects approximately 700 million individuals across 50 nations, with projections indicating that by 2025, over 1.5 billion people will confront the challenges posed by this issue [3]. Hence, it is imperative to expedite the development of an efficient and dependable water purification technology. So far, conventional physical and chemical processes, including adsorption, coagulation, oxidation, and membrane techniques, have emerged as the primary approaches and experimental methods for industrial wastewater treatment [4–11]. While traditional wastewater treatment methods have been shown to be effective in removing organic dyes, their effectiveness is limited when dealing with complex chemical structures. Therefore, there has been considerable research interest in developing novel technologies that can overcome these limitations and improve the efficiency of dye-contaminated wastewater treatment. Among these wastewater treatment technologies, adsorption, photocatalysis and membrane processes are showing encouraging results.

Photocatalytic oxidation, a water treatment process that emerged in the 1970s, has attracted considerable attention due to its potential for the efficient and sustainable removal of pollutants from wastewater [12]. The incorporation of catalysts into photocatalytic oxidation systems not only enables milder reaction conditions and a significant reduction in engineering costs but also facilitates the complete degradation of organic pollutants, achieving complete mineralization and greatly increasing the removal efficiency. Typically, n-type semiconductor materials are used as photocatalysts [13]. Commonly used photocatalysts include TiO_2, ZnO, Fe_2O_3, SnO_2, WO_3, and CdS. TiO_2 is widely utilized in various photocatalytic processes due to its exceptional thermal stability, cost-effectiveness, and high photocatalytic activity [14]. TiO_2 is a semiconducting material that has a discontinuous energy band structure resulting from the hybridization of Ti 3d and O 2p orbitals. The band structure of TiO_2 consists of valence, conduction, and forbidden bands. When TiO_2 is exposed to light, electrons (e^-) in the valence band are excited to the conduction band through the forbidden band, leaving behind holes (h^+). This process is governed by the photoelectric effect [15]. After the excitation of the electrons in the valence band, there are two forms: some excited photoelectrons will be captured by the defect sites of TiO_2, and the others will be captured by holes, at which time the energy is released in the form of heat. At this point, the efficient separation of holes and electrons is achieved, which is the main factor affecting photocatalytic efficiency [16]. Subject to electric field forces, photogenerated charge carriers migrate to different locations in the semiconductor and react with O_2 or H_2O on the TiO_2 surface to produce reactive oxygen species and hydroxyl radicals, which are highly oxidizing and are the main factors in achieving photocatalysis. In addition to TiO_2, other photocatalysts and biomimetic photocatalysts have been investigated for their potential use in water treatment applications [17,18]. Despite their potential, photocatalysts suffer from limitations such as wide band gaps, resulting in limited absorption of photons, low light harvesting efficiencies, stringent light source requirements, and high recombination rates of photogenerated electron-hole pairs during the reaction process. These factors contribute to low photon utilization and catalytic efficiency, resulting in sub-optimal processing results.

Due to their extensive specific surface area, porosity, and diverse structural forms (including carbon isomers such as AC, graphene, carbon nanotubes, fullerenes, diamond, and coal), carbon-based materials find widespread applications in various fields including aerospace engineering, supercapacitors technology, catalysis research, adsorption research, and renewable energy systems [19–24]. AC, as a type of carbon allotrope, is characterized by its superior porosity compared with other carbon forms. Its unique combination of mesopores and micropores enables it to effectively adsorb large liquid molecules through the mesopores and trap small gas molecules through the micropores. This property makes AC a highly versatile material for various applications, including supercapacitors, energy storage devices, and gas separation membranes [25,26]. However, the removal of pollutants by AC alone still has some shortcomings [27–29]. As is well known, after adsorption saturation, AC needs to be exposed to excessive sunlight and other treatments to restore its adsorption performance, which may also cause secondary pollution to the environment in the process, and to achieve the desired effect of pollutant removal, long adsorption times are required [30,31].

Herein, TiO_2 was successfully loaded onto AC by a simple ultrasonic impregnation technique. This method realizes the synergistic degradation of organic pollutants and at the same time solves the problem that titanium dioxide powder is difficult to separate and recycle for reuse. Notably, the TiO_2/AC with the content of TiO_2 reaching 3 wt% exhibits the optimal synergistic adsorption and photocatalysis rate of 99.6 % for 100 mg/L of MB. The high specific area of activated carbon in the composite increases both the local concentration around the catalyst and the contact area of TiO_2 with the pollutant, thereby favoring the complete degradation of the intermediate. Furthermore, the photocatalytic performances of the composites has been found to be positively correlated with the pore size, pore volume, and specific surface area of the AC. Therefore, the use of highland barley straw as a source of AC would be a promising alternative carbon carrier for photocatalysts. From the perspective of the circular economy, the approach of converting waste into resources and achieving their reuse and regeneration not only enables the sustainable development of mesoporous carbon materials but also brings new ideas and opportunities for local economic development.

2. Materials and methods

2.1. Materials

Citric acid ($C_6H_8O_7$, ≥99.5 %), tetrabutyl titanate ($C_{16}H_{36}O_4Ti$, 98.0 %), and potassium hydroxide (KOH, 99.99 %) were purchased from Shanghai Aladdin Company. Methylene blue ($C_{16}H_{18}ClN_3S$, ≥98 %) was purchased from Solarbio Shanghai Fuze Trading Co. Anhydrous ethanol (CH_3CH_2OH, ≥99.8 %) was purchased from Shanghai Maclean Biochemical Technology Co. Hydrochloric acid (HCl, 37 %), was purchased from Guangdong Guanghua Chemical Company (Guangzhou, China). Additionally, all the solutions were prepared with deionized water throughout the experiment.

2.2. Preparation of activated carbon (AC), TiO_2, and TiO_2/AC composites

The highland barley straw powder after the hydrothermal reaction was mixed with a citric acid solution of a specified concentration in a mass ratio of 1:10. The hydrothermal reaction was carried out for 120 min at a temperature of 240°C. The resulting AC precursor was then mixed with potassium hydroxide as an activator in a mass ratio of 1:1. The mixture was impregnated for a period of time and then dried in an oven at 105°C for 24 h. High-temperature-assisted activation was carried out by setting different temperature parameters in a tube furnace for 1 h. The results showed that AC with a specific surface area of 1906.1266 m^2/g was prepared at 1100 °C [32].

Next, 50 mL of anhydrous ethanol was mixed with 4 mL of concentrated hydrochloric acid, 25 mL of tetrabutyl titanate was added, and the mixture was stirred for 10 min. The mixture was heated at 150°C for 6 h in a reaction vessel, and then it was dried and ground to obtain the desired TiO_2 [33].

TiO_2 dispersions with different mass fractions (1, 2, 3, 4, and 5 wt%) were prepared using home-made TiO_2 nanoparticles. The TiO_2 nanoparticles were uniformly dispersed in deionized water through a 20 min ultrasonication process. Subsequently, 50 mL aliquots of each TiO_2 dispersion were taken and combined with 1 g of pre-prepared activated carbon in separate beakers. The ultrasonication process was repeated for 60 min under a controlled temperature atmosphere of 60°C. Afterward, the composite materials were washed three times with ultrapure water and dried. It is worth noting that the TiO_2 used in this study possesses the characteristic of long-term stable dispersion in deionized water, avoiding any precipitation that could impact the composite material's properties. The mechanism of TiO_2/AC composites preparation is described by equations (1)–(3).

$$TiO_2 \text{ nanoparticles} + H_2O \text{ (deionized)} \overset{\text{ultrasonication}}{\rightarrow} \text{Uniform } TiO_2 \text{ dispersion} \quad (1)$$

$$TiO_2 \text{ dispersion} + \text{Activated Carbon} \xrightarrow{\text{ultrasonication}} TiO_2 \,/\, \text{Activated Carbon composite} \quad (2)$$

$$TiO_2 \,/\, \text{Activated Carbon composite} + H_2O \text{ (ultrapure)} \xrightarrow{\textit{washing+drying}} \text{Dry } TiO_2 \,/\, \text{Activated Carbon composite} \quad (3)$$

2.3. Sample characterization

The structural properties and morphologies of the prepared TiO_2/AC composites were observed by field-emission scanning electron microscopy (SEM, 30-kV acceleration voltage). To determine the crystal phase composition, X-ray diffraction measurements were carried out at room temperature using a BRUCKER D8 ADVANCE in the 2θ range of 10°–90°. Transmission electron microscopy (TEM, FEI Talos F200X) was used to observe the microstructures of the samples. The elemental compositions and chemical bonds of the prepared samples were characterized by X-ray photoelectron spectroscopy (XPS, Thermo Scientific Escalab 250Xi). Nitrogen adsorption–desorption analysis was carried out using the Brunauer–Emmett–Teller (BET, ASAP 2460 Surface Area and Pressure) method to determine the specific surface area of each sample. Functional group analysis of the TiO_2/AC composites was performed using Fourier transform infrared spectroscopy (FTIR) in the 4000–400 cm^{-1} region. Raman characterization of the structural composition of the TiO_2/AC composites was performed using a Renishaw Raman Horiba spectrometer with a laser wavelength of 532 nm^{-1}. The concentration of dye ions was determined by ultraviolet–visible (UV–vis) spectroscopy with a maximum wavelength of 664 nm.

2.4. Co-sorption photocatalysis experiments

To investigate the decontamination performance and stability of the composite, six groups of control experiments were conducted. Firstly, a 300 mL solution of MB with a concentration of 100 mg/L was prepared and evenly divided into six groups, each containing 50 mL. Subsequently, samples with different mass ratios of TiO_2 prepared in 2.2 were sequentially added to six sets of 50 mL MB solutions, i.e., 1 g of AC, 1 g of TiO_2/AC (1 wt%), 1 g of TiO_2/AC (2 wt%), 1 g of TiO_2/AC (3 wt%), 1 g of TiO_2/AC (4 wt%) and 1 g of TiO_2/AC (5 wt%), respectively. The dispersed solution was placed in a photocatalytic reaction chamber. And then it was irradiated for 100 min using a 300-W xenon lamp. Throughout the experiment, the distance between the radiation source and the solution was consistently maintained at 10 cm. The removal rate in the study was calculated using equation (4):

$$\text{Removal efficiency} = \frac{C_o - Ct}{C_0} \times 100\%, \quad (4)$$

where C_0 and C_t are the concentrations of MB in solution (mg/L) at the initial time and at any time t, respectively. The photocatalytic degradation data were then fitted using the following pseudo-first-order kinetics equation (equation (5)) [34]:

$$-\ln(C_t / C_0) = kt, \quad (5)$$

where k is the pseudo-first-order rate constant. Photodegradation cycling tests were performed on the best TiO_2/AC (3 wt%) sample under the same reaction conditions to determine the stability and reusability of the photocatalyst.

To investigate the cycling properties of the composites: a 100 mg/L solution of MB at pH = 7 was prepared with a controlled reaction time of 100 min and a reaction temperature of 308 K. TiO_2/AC (3 wt%) was chosen for the test. After the last cycle, the nanocomposites were collected, washed with 0.1 mol/L HCl, and then washed with excess deionized water to neutralize and dried for the next cycle. The removal performance of the nanocomposites was tested after five cycles.

3. Results and discussion

3.1. Structural analyses

Fig. 1 shows the XRD spectra of the TiO_2/AC nanocomposites. The peak observed at approximately 24° corresponded to amorphous carbon, indicating that the AC had a graphite-like structure. The diffraction peak of TiO_2 appeared at 25.41°, corresponding to the (101) face of anatase, as well as at 71.48°, corresponding to the (220) face of rutile. These results suggest that the TiO_2 in question was a mixed crystalline form of rutile and anatase (JCPDS PDF #:00-021-1245) [35]. With an increase in the amount of TiO_2 in the composite, the peaks of AC were gradually covered, clear rutile and anatase TiO_2 diffraction peaks appeared, and a crystalline phase emerged. A gradual increase in the sizes of the diffraction peaks of rutile and anatase crystals occurred for the loading levels of 2–4 wt %. Instead, at 5 wt%, the size of the diffraction peak decreased and the crystallinity began to decrease. This was a result of the high TiO_2 content, which could not be compounded on the AC. From the Scherrer equation (equation (6)) [36], given as follows, it was determined that TiO_2/AC (3 wt%) had the smallest crystal size and was more uniformly distributed than other mass fractions of TiO_2:

$$D = K\lambda/\beta \cos\theta, \quad (6)$$

where D (nm) is the grain size, K is the Scherrer constant, β represents the half-height width, and θ is the Bragg diffraction angle.

Fig. 2 displays the SEM micrographs of the AC and TiO_2/AC nanocomposites. As the mass fraction of TiO_2 increased, TiO_2 particles gradually accumulated on the outer surface of the AC, leading to pore clogging. The surface structure of AC was rough and porous, as depicted in Fig. 2a. However, as the loading of TiO_2 increased, the pores of the AC were gradually covered, as shown in Fig. 2b–f. The average particle size of the TiO_2 used in this study was in the range of 10–40 nm, classifying it as nanoscale TiO_2. It shows the uniform distribution of TiO_2 particles on the surface of the AC. Some larger TiO_2 particles were also present in the composite shown. These results suggested that the higher free energy of the TiO_2 particles in the nano-system led to lower relative stability, resulting in particle aggregation due to inherent instability [37]. Therefore, relatively large particles of TiO_2 appeared in the SEM image. Furthermore, with an increase in the mass fraction of TiO_2, there was an increase in the amount of TiO_2 dispersed on the AC surface, which could provide a sufficient quantity of photocatalytic radicals. Once the loading of TiO_2 surpassed a certain threshold, the porous characteristics of the AC became obstructed, leading to a decrease in its specific surface area. This, in turn, could compromise the original

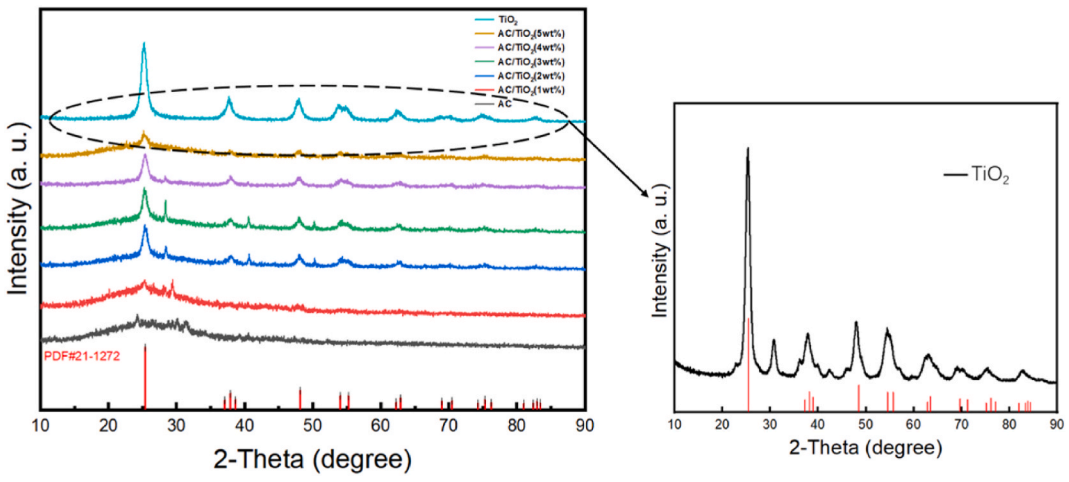

Fig. 1. XRD patterns of the xTiO_2/AC (x = 1 wt%, 2 wt%, 3 wt%, 4 wt%, and 5 wt%) catalysts (a) and self-made TiO_2 (b).

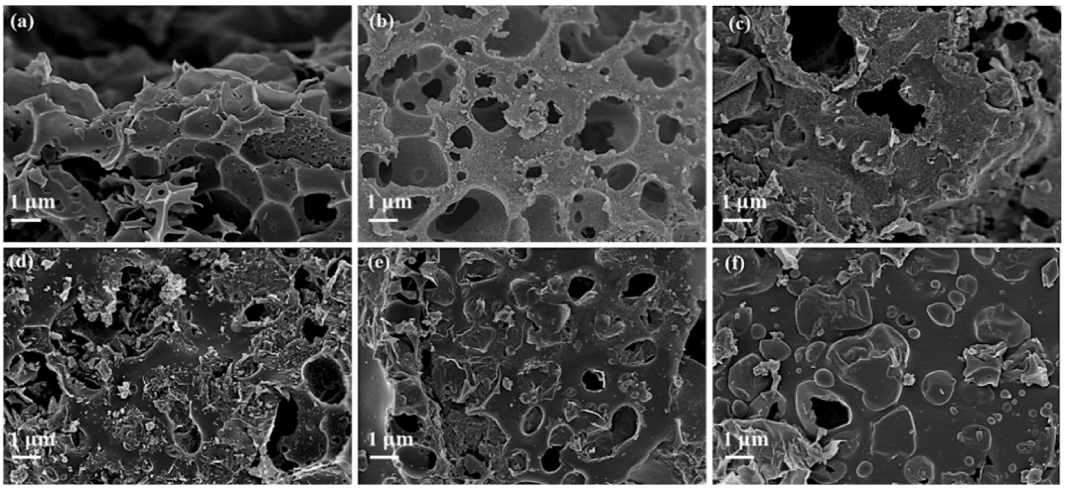

Fig. 2. SEM images of (a) AC; (b) TiO_2/AC (1 wt%); (c) TiO_2/AC (2 wt%); (d) TiO_2/AC (3 wt%); (e) TiO_2/AC (4 wt%); and (f) TiO_2/AC (5 wt%).

adsorption properties of the AC.

The BET analysis results of the various adsorbents are presented in Fig. 3. The horizontal axis displays the different samples, with A, B, C, D, E, and F representing AC, TiO_2/AC (1 wt%), TiO_2/AC (2 wt%), TiO_2/AC (3 wt%), TiO_2/AC (4 wt%), and TiO_2/AC (5 wt%), respectively. As depicted in Fig. 3b, the AC possessed a specific surface area of 1374.56 m^2/g. With the addition of TiO_2 with mass fractions of 1–5 wt%, the specific surface area decreased to 605.34, 454.52, 310.03, 235.78, and 223.43 m^2/g. The incorporation of TiO_2 in the AC composite resulted in a significant reduction in the specific surface area compared with that of the AC without TiO_2. As the mass fraction of the TiO_2 increased to 5 wt%, the specific surface area decreased to 223.43 m^2/g, which was approximately one-sixth of the original AC specific surface area. Excess TiO_2 was dispersed on the surface of the AC, covering its pores and blocking its original pore size.

According to Fig. 3a, the variation in the pore size of the AC remained constant at around 3.45 nm, regardless of the quantity of TiO_2 added. Fig. 3c shows that as the amount of TiO_2 increased, there was a corresponding decrease in the average pore volume from 0.50 to 0.22 cm^3/g. This trend was similar to that observed for the specific surface area, as shown in Fig. 3b. The reduction in the pore volume would have an effect on the adsorption capacity of the AC, as it would mainly promote the movement of the adsorbent on the surface of the AC and increase the adsorption capacity during the removal of pollutants. The analytical results shown here were consistent with the results found by SEM.

Fig. 4 shows a TEM image of the self-made TiO_2. Fig. 4a shows a TEM image of TiO_2 at a magnification scale of 200 nm, where the TiO_2 nanoparticles are clearly visible. The high-resolution transmission electron microscopy (HR-TEM) image in Fig. 4b reveals a lattice spacing of d = 0.352 nm, which is close to that of the (101) surface of TiO_2 (JCPDS #71–1168) [38]. As shown in Fig. 4c, the diffraction pattern of TiO_2 exhibited multiple rings, indicating that the sample was composed of polycrystalline grains with different crystallographic orientations. The diffraction rings corresponded to the constructive interference between X-rays and the crystal planes in each individual grain, providing valuable information about the crystal structure and orientation distribution of the material. Fig. 4d shows the high-angle annular dark field image. Fig. 4e and f present the energy dispersive X-ray spectroscopy (EDS) patterns, which provided insights into the spatial distributions of Ti and O within the sample. The TEM images, in combination with the XRD analysis, unequivocally confirmed that the TiO_2 synthesized under these experimental conditions was a polycrystalline material composed of both anatase and rutile phases.

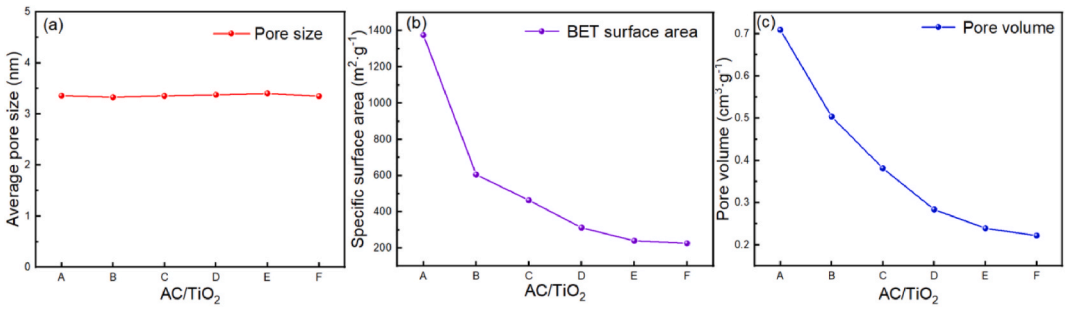

Fig. 3. Specific surface area of AC and xTiO_2/AC (x = 1 wt%, 2 wt%, 3 wt%, 4 wt%, and 5 wt%) catalysts: (a) pore size, (b) specific surface area, and (c) pore volume.

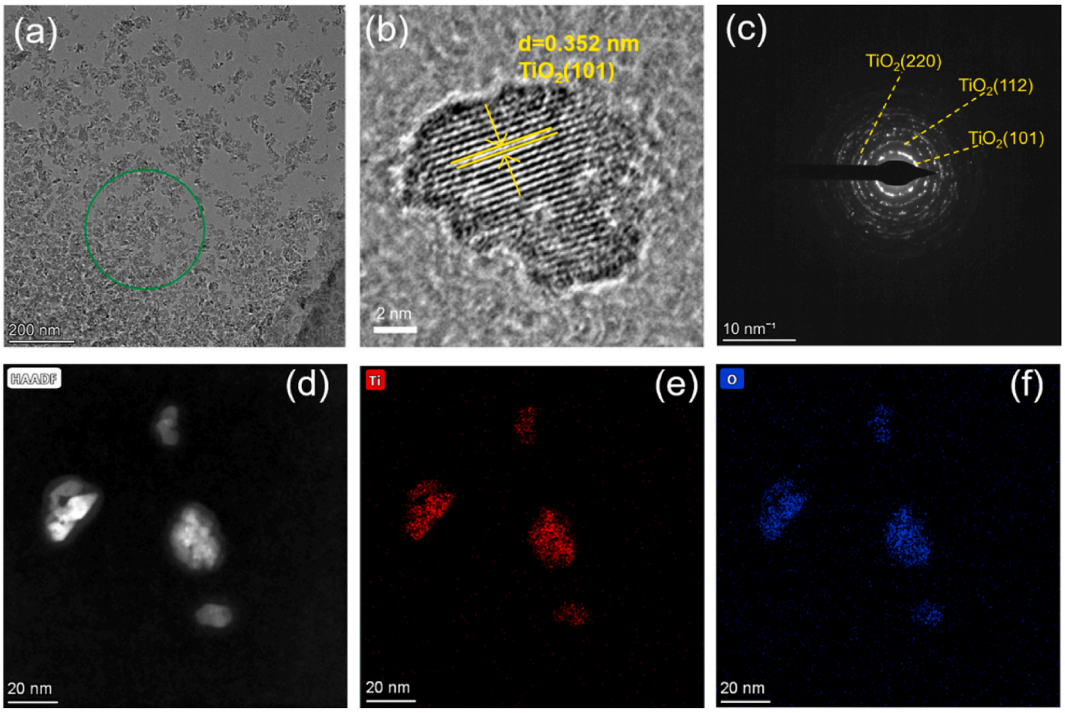

Fig. 4. (a) TEM images of self-made TiO_2; (b) HRTEM images of self-made TiO_2; (c) SAED images of self-made TiO_2; (d) HAADF images of self-made TiO_2; (e–f) the EDX elemental mappings of self-made TiO_2.

Fig. 5 shows the microstructure and composition of the TiO_2/AC. Fig. 5a displays a TEM image of the TiO_2/AC composite material at a magnification scale of 100 nm. The dispersion of the TiO_2 nanoparticles within the AC structure was evident from the results, indicating a uniform distribution of the nanoparticles throughout the carbon matrix. This high degree of dispersion was attributed to the strong interactions between the TiO_2 particles and the carbon surface, which enhanced their stability and prevented agglomeration. The HR-TEM image shown in Fig. 5b reveals distinct striated features that were attributed to the presence of amorphous carbon

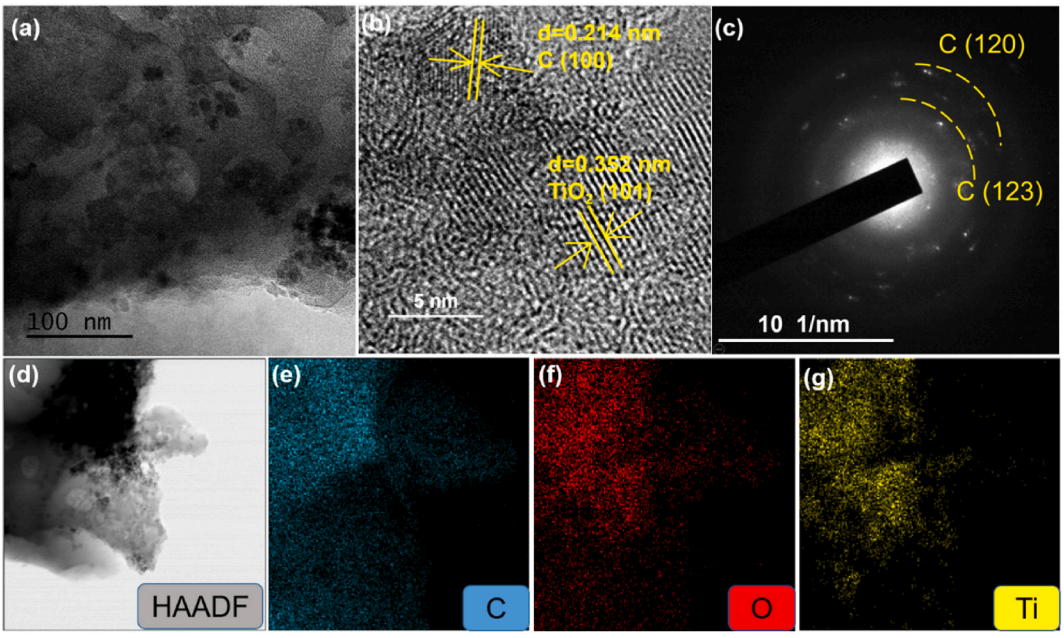

Fig. 5. (a) TEM images of TiO_2/AC nanocomposites; (b) HRTEM images of TiO_2/AC nanocomposites; (c) SAED images of TiO_2/AC nanocomposites; (d) HAADF images of TiO_2/AC nanocomposites; (e–f) the EDX elemental mappings of TiO_2/AC nanocomposites.

structures with the crystalline spacing of TiO_2, including both rutile and anatase phases. The measured layer spacing of 0.214 nm at the interfacial region was consistent with the (100) plane spacing of graphite (JCPDS #41–1487) [39,40]. Combined with Fig. 1, the XRD pattern showed a diffraction peak at $2\theta = 25.3^{\circ}$, corresponding to a d-spacing of 0.352 nm, which was assigned to the (101) plane of anatase TiO_2 (JCPDS #91–1167) [39,40]. This result confirmed that the synthesized material was a composite of AC and TiO_2. The polycrystalline nature of the complex was further supported by the presence of the C(120) and C(123) planes observed in the selected area electron diffraction (SAED) pattern shown in Fig. 5c. Fig. 5d shows the high-angle annular dark field image. The elemental distributions in the TiO_2/AC composite materials were analyzed using EDS, as shown in Fig. 5e–g. The profiles indicated that the distributions of C, Ti, and O were uniform throughout the sample, which suggested that the composite material was mainly composed of a carbon skeleton with a graphite-like structure and polycrystalline TiO_2. This result confirmed the successful synthesis of the TiO_2/AC composite material with a well-defined composition and structure.

The functional groups present in the TiO_2/AC composite were identified and quantified using Fourier-transform infrared (FTIR) spectroscopy. As shown in Fig. 6a, the composites exhibited seven distinct absorption bands in the 4000–400 cm^{-1} region, which were attributed to the different functional groups present on the AC. These bands provided valuable information about the structural and chemical properties of the composites [41–43]. In each spectrum, the peak at 3435.01 cm^{-1} was attributed to the stretching vibrations of the $–NH_2$ bonds. The absorption peak at around 1750 cm^{-1} was due to the stretching vibrations of C=O [44]. The peak near 1350 cm^{-1} was the characteristic absorption peak caused by the deformation of –OH groups. In the range of 1000–900 cm^{-1}, the absorption band was formed by the stretching of the C–C skeleton [45]. With the increase in the amount of TiO_2, the size of the infrared absorption peak resulting from the C=O stretching vibrations gradually diminished. This suggested that the C=O groups were being covered by Ti=O and that the TiO_2 coated the AC surface. These findings agreed with those presented in Figs. 1 and 5.

The Raman spectrum of the TiO_2/AC composite with loadings of 3 wt% is shown in Fig. 6b, which confirms the presence of graphitic carbon in the composite. This finding is consistent with the X-ray diffraction analysis presented in Fig. 1. The Raman spectrum of the TiO_2/AC composite exhibited two distinct peaks at 1365 and 1592 cm^{-1}, which can be attributed to the D-band and G-band peaks, respectively. The appearance of D-band peaks in the Raman spectra can be attributed to the disorder within the AC, which resulted from defects and sp^3 hybridization of carbon atoms in the carbon structure. The presence of G-band peaks in the Raman spectra was attributed to the sp^2 carbon atoms in the hexagonal bonds of the graphite network. Specifically, all the sp^2 atom pairs within the carbon ring or chain contributed to the production of G peaks. The I_D/I_G ratio, which represents the intensity of the D-band peak relative to the G-band peak in the Raman spectrum of the TiO_2/AC composite, was found to be 0.507. This indicated a high level of graphitization in the material [46]. This study demonstrated that composites synthesized under these conditions possessed high purity, structural stability, and they exhibited efficient electron transport on the AC surface, leading to enhanced photocatalytic performances of the composites.

To provide further evidence for the successful deposition of TiO_2 onto the AC surface, detailed X-ray photoelectron spectra of the TiO_2/AC composite with loadings of 3 wt% were collected, as shown in Fig. 7. Based on the X-ray photoelectron spectra analysis presented in Fig. 7a, it can be inferred that the TiO_2/AC composite was predominantly composed of carbon, titanium, and oxygen. Fig. 7b displays the deconvoluted C1s spectrum of the anti-fold product, revealing three prominent peaks corresponding to C–H, C–C, and C–O functional groups. The relative intensity of the C–C peak suggested that the AC in the TiO_2/AC composite possessed a graphite-like carbon structure. The O1s spectrum in Fig. 7c had a peak at around 239 eV, which indicated the presence of metal oxides, specifically Ti=O. In addition, the C–O peak observed at 530.8 eV confirmed that the C1s orbital originated from the valence state identified in Fig. 7b. Fig. 7d displays the binding energy region associated with both the Ti2p 3/2 and Ti2p 1/2 states, which originated from TiO_2 [47]. The symmetric peaks and high intensity observed in this region corresponded to the Ti2p orbital of TiO_2. The XPS measurements corroborated the FTIR findings outlined earlier, providing additional evidence for the structural composition of the TiO_2/AC composites.

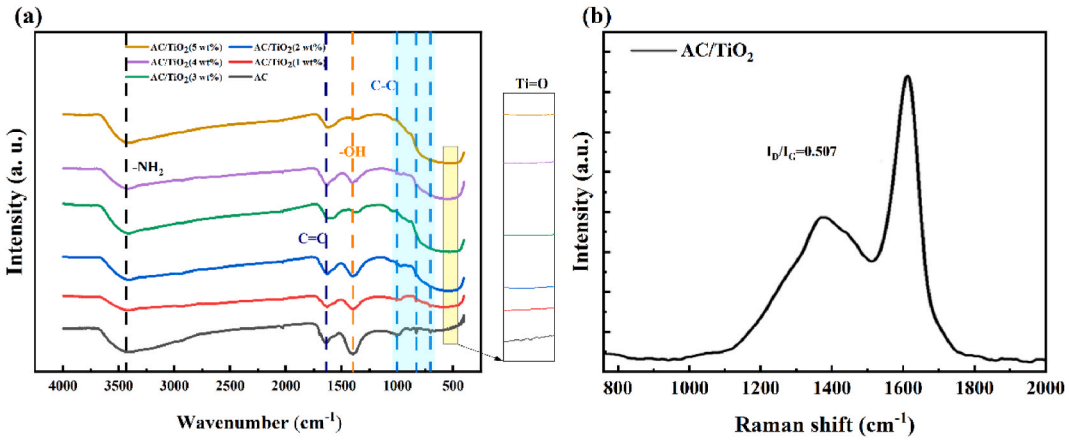

Fig. 6. (a) FT-IR spectra of AC and xTiO_2/AC (x = 1 wt%, 2 wt%, 3 wt%, 4 wt%, and 5 wt%) catalysts; (b) Raman spectra of xTiO_2/AC (x = 3 wt%).

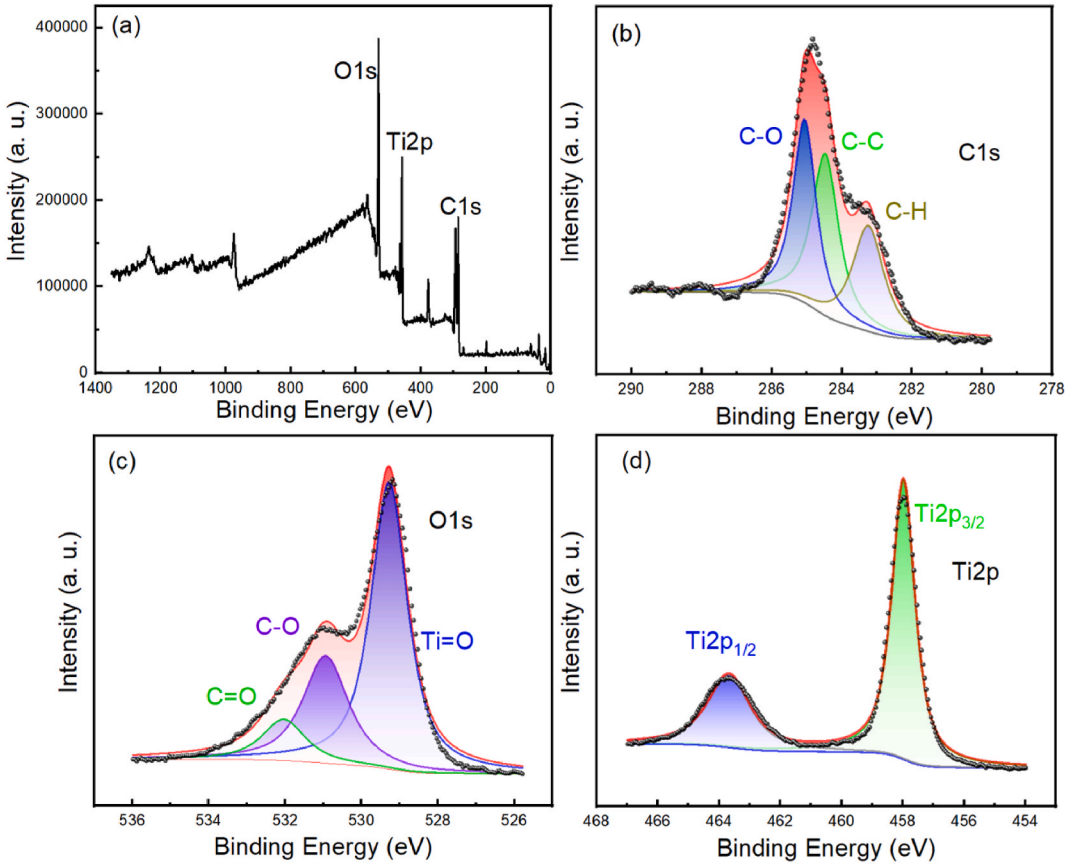

Fig. 7. (a) XPS spectra, (b) C 1s, (c) O 1s, and (d) Ti 2p of the $xTiO_2$/AC(x = 3 wt%).

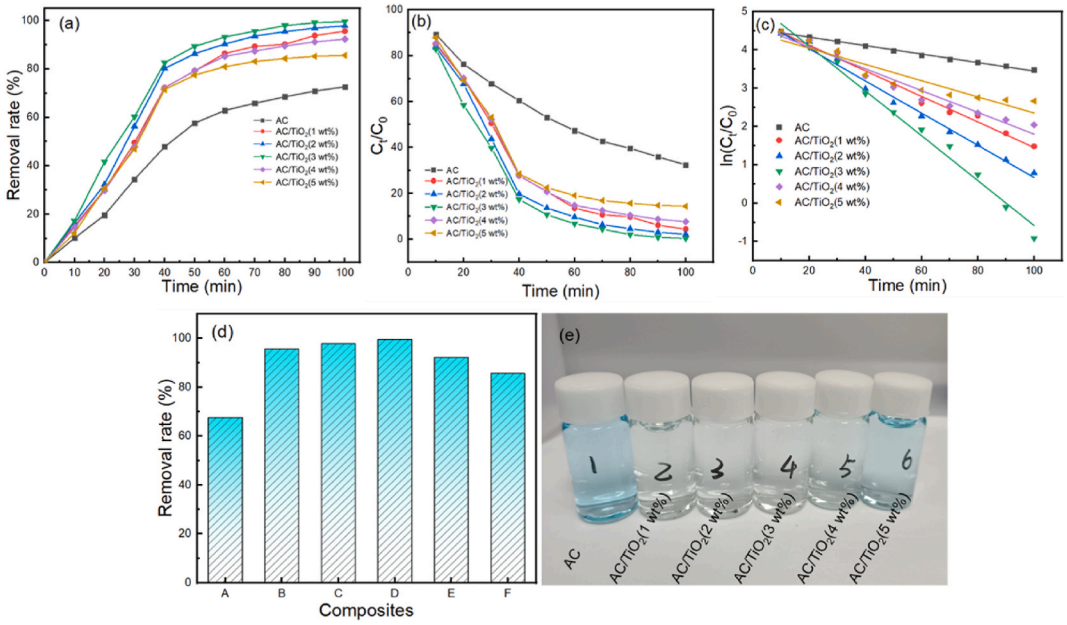

Fig. 8. Synergistic degradation of MB by AC and TiO_2/AC nanocomposites: (a) removal rate, (b, c) kinetics curves of synergistic degradation of MB, (d) degradation rate, and (e) schematic of degradation.

3.2. Degradation of methylene blue by TiO_2/AC nanocomposites

To assess the decontamination efficacy and stability of the composite material, a series of experiments were carried out. The results are shown in Fig. 8. The horizontal coordinates A, B, C, D, E, and F in Fig. 8d represent AC, TiO_2/AC (1 wt%), TiO_2/AC (2 wt%), TiO_2/AC (3 wt%), TiO_2/AC (4 wt%), and TiO_2/AC (5 wt%), respectively. Fig. 8a and d shows the removal rates of the six sample groups at 100 min, which were found to be 72.6%, 95.6%, 97.8%, 99.6%, 92.3%, and 85.6%, respectively. The removal rates of the six sample groups gradually decreased over time. This is likely due to the decreasing MB content in the solution, which prevented TiO_2 from fully participating in the photocatalysis, resulting in a slower removal rate after 40 min. The composite materials exhibited higher MB removal efficiencies before 40 min compared with that of the AC alone due to the synergistic effect of both the photocatalytic properties of TiO_2 and the adsorption properties of AC. The TiO_2/AC composites exhibited higher removal efficiencies of MB than TiO_2 alone after 40 min, likely due to the synergistic effect of AC and TiO_2. The AC provided a porous structure that allowed for the efficient adsorption of MB, while the TiO_2 facilitated photocatalytic degradation of the dye. This combination resulted in more complete contact between the composite material and MB, leading to relatively efficient removal. This finding suggested that the composite material has promising potential for efficient wastewater treatment.

Fig. 8d shows the MB degradation rates for five composites. The highest removal rate was observed when the TiO_2 composite had a loading of 3 wt%. However, as the loading increased beyond this point, the removal rate began to decrease instead. Fig. 8e presents a real-life image of MB degradation by five types of composite materials. A clear and transparent liquid is observed when the TiO_2 composite material has a loading of 3 wt%. When the content is below or above 3 wt%, a blue liquid is visible. The analysis suggested that the reduced adsorption performance of AC, due to its reduced specific surface area, may have been one reason that TiO_2 was unable to fully contact MB after 40 min. The second reason for the reduced photocatalytic efficiency was the excessive amount of TiO_2, which led to a decrease in the light transmission rate. Consequently, the generation of free hydroxyl groups and active oxygen by TiO_2 was insufficient, resulting in a decrease in the photocatalytic efficiency. Fig. 8c shows the kinetics curves for the adsorption and degradation of AC and TiO_2/AC. To quantitatively compare the pollutant removal efficiencies of the different composites, the photocatalytic degradation data were fitted using a pseudo-first-order kinetics equation. ln (C_t/C_0) for the six composites had a good linear relationship with time t and was consistent with first-order reaction kinetics. The reaction rates k for the six materials were calculated using the pseudo-first-order kinetics equation, with values of 0.0111, 0.0334, 0.0420, 0.0585, 0.0284, and 0.0212 min^{-1} obtained for the AC and TiO_2/AC composites with loadings of 1, 2, 3, 4, and 5 wt%, respectively (as shown in Table 1). The magnitude of k reflects the pollutant removal rate, and our results indicate that the highest pollutant removal rate was achieved at a mass fraction of 3 wt% for the TiO_2 composites. Considering of our harsh evaluation condition by using 1 g of TiO_2/AC to treat 50 mL of MB solution (100 mg/L) within 100 min, the resultant TiO_2/AC heterojunction possess better removal efficiency for MB than most of the semiconductor-based materials listed in Table 2.

The cyclic performance of a composite is a crucial practical indicator that reflects its stability and durability over time. Therefore, it was essential to investigate the cyclic stability of the TiO_2/AC composite to evaluate its potential for real-world applications. The cycling performance test results are shown in Fig. 9a. After cycles 1–5, the TiO_2/AC (3 wt%) exhibited an excellent removal performance, with removal rates of 99.6%, 97.8%, 93.5%, 87.3%, and 83.1% respectively. Despite the slight decrease in the decontamination efficiency after five cycles, the overall effectiveness of the material remained similar, suggesting its potential for repeated use in wastewater treatment to remove pollutants.

The FTIR absorption spectrum of TiO_2/AC (3 wt%) after five cycles is presented in Fig. 9b. The measured data provide insight into the chemical structure and composition of the material following multiple regeneration cycles. The findings are consistent with those presented in Fig. 6a, which demonstrated that the TiO_2/AC (3 wt%) possessed both robust structural integrity and notable catalytic activity. These results collectively indicate the reusability of the material for the effective removal of pollutants from wastewater.

3.3. Mechanism

The decontamination mechanism of the composite was attributed to a synergistic effect between highland barley straw AC adsorption and the TiO_2 photocatalysis, as shown in Fig. 10. Firstly, activated carbon adsorbed MB molecules by physical adsorption and chemical adsorption. Due to its significant surface area and porosity, AC physically adsorbs MB molecules driven by van der Waals forces. Then it is promoted by hydrogen bonding or π-π interaction between the aromatic rings of AC and MB, so that chemisorption occurs simultaneously. Under the strong adsorption of AC, the pollutants are fixed on the surface of the composite material, which increases the concentration of pollutants around TiO_2. In the photocatalytic degradation process, AC can act as an electron acceptor, reducing the recombination rate of electrons and holes, thus making more of them available for photocatalytic reactions. AC can also increase the dispersion of TiO_2 particles, exposing more active sites for the photocatalytic reaction. Upon illumination with light of sufficient energy, TiO_2 generates electron-hole pairs. The electrons can reduce oxygen to form superoxide radicals ($\cdot O_2^-$), while the holes can oxidize water or hydroxide ions to form hydroxyl radicals (· OH). These ROS are highly reactive and capable of degrading MB molecules adsorbed on the surface of the composite breaking down their chemical structure into smaller, less harmful compounds until complete mineralization to CO_2, H_2O, and inorganic ions is achieved. The final degradation products have a lower molecular weight and are less likely to adsorb onto the surface of AC or TiO_2. Consequently, these products desorb from the photocatalyst surface, freeing up sites for the adsorption of more MB molecules and maintaining the efficiency of the photocatalytic process. The combined action of TiO_2 and AC in the TiO_2/AC composite not only captures MB molecules more effectively through adsorption but also degrades them more efficiently under light irradiation due to enhanced charge separation, increased catalytic sites, and the generation of reactive

Table 1
Comparison of the rate constants (k) of the composites.

Sample	k (min^{-1})	R [2]
AC	0.0111	0.9934
TiO_2/AC (1 wt%)	0.0334	0.9865
TiO_2/AC (2 wt%)	0.0420	0.9895
TiO_2/AC (3 wt%)	0.0585	0.9869
TiO_2/AC (4 wt%)	0.0284	0.9603
TiO_2/AC (5 wt%)	0.0212	0.8867

Table 2
Elimination efficiency of the semiconductor-based materials for MB dyes.

Material	Power of Xenon lamp (W)	Time (min)	Elimination Efficiency (%)	The dosage of the material (mg)/amount of MB solution (mL) × MB concentration (mg L^{-1})	Ref.
TiO_2/g-C_3N_4	160	100	98.5	20/100 × 5	[48]
RS-HTO	300	90	95.18	200/100 × 10	[49]
CeO_2/TiO_2	250	120	100	80/100 × 15	[50]
Banana peel activated carbon-TiO_2	/	/	94.61	500/25 × 30	[51]
WO_3/AC	15-25 ($mWcm^{-2}$)	25	94	20/20 × 10	[52]
TiO_2/AC	300	100	99.6	1000/50 × 100	This work

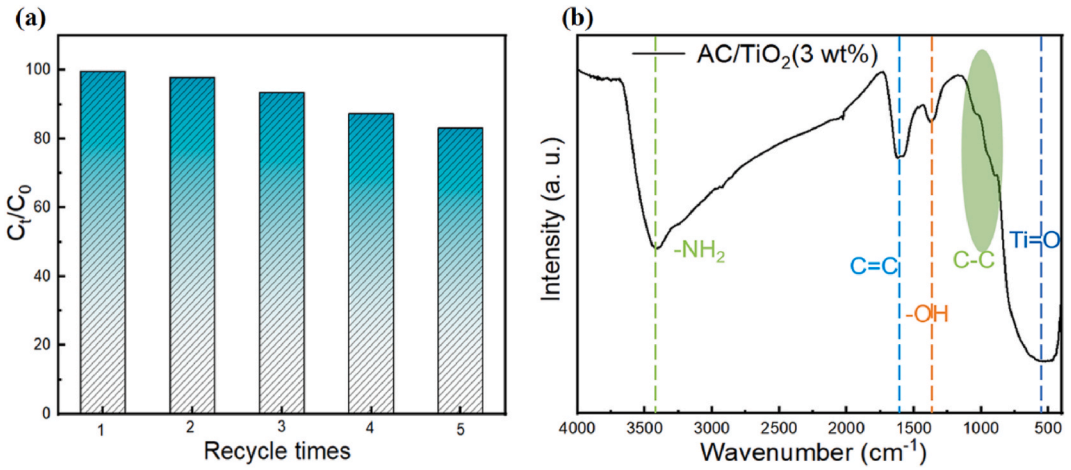

Fig. 9. (a) TiO_2/AC (3 wt%) degradation of MB over five cycles. (b) FT-IR spectra of TiO_2/AC (3 wt%) sample after recycling.

oxygen species. This synergistic effect makes TiO_2/AC an effective photocatalyst for the degradation of organic pollutants like Methylene Blue.

4. Conclusion

AC was prepared successfully from highland barley straw through a chemical activation method with KOH followed by a calcination process. The loading of TiO_2 onto pre-prepared activated carbon (AC) was carried out. Successful preparation of TiO_2/AC nanocomposites with stable synergistic adsorption and photocatalysis characteristics was achieved. Furthermore, we assessed the synergistic adsorption and photocatalytic efficacy of the TiO_2/AC nanocomposites for the degradation of methylene blue (MB) in industrial wastewater. We successfully elucidated the effect of AC carriers on the photocatalytic reaction of TiO_2, using various analytical techniques, such as scanning electron microscopy (SEM), Fourier-transform infrared spectroscopy (FTIR), surface area analysis, and transmission electron microscopy (TEM). The characterization results revealed that the TiO_2 particles were uniformly distributed on the AC support, with both anatase and rutile phases present. Through parameter studies, it was found that under natural light irradiation, the synergistic degradation of 100 mg/L MB was achieved with a dye degradation efficiency of 99.6 % within 100 min. These results demonstrated the excellent synergistic adsorption and photocatalytic properties of TiO_2/AC, making it an efficient and effective catalyst for degrading organic pollutants. This method has the potential for application in the treatment of industrial organic pollutants in water.

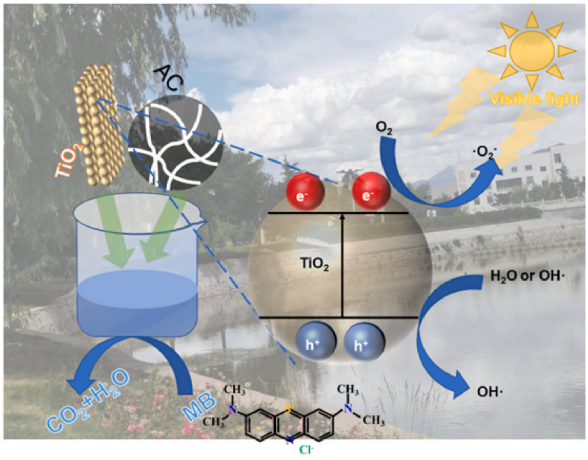

Fig. 10. Schematic illustration of MB removal by TiO_2/AC.

Funding

This work was supported by the National Natural Science Foundation of China (Grant No: 52062045), Central Government Funds for Local Scientific and Technological Development (Grant No: XZ202101YD0019C), Natural Science Foundation of Tibet Autonomous Region (Grant No. XZ202301ZR0020G).

Data availability statement

All data to support the conclusions have been either provided. Data included in article.

CRediT authorship contribution statement

Yihang Yue: Writing – original draft, Methodology, Investigation, Data curation, Conceptualization. **Xiaoju Yue:** Writing – review & editing, Writing – original draft, Investigation, Data curation, Conceptualization. **Xiaofeng Tang:** Writing – review & editing, Resources, Formal analysis. **Lin Han:** Formal analysis. **Jinnong Wang:** Formal analysis. **Shifeng Wang:** Writing – review & editing, Supervision, Project administration, Funding acquisition. **Chun Du:** Supervision, Project administration.

Declaration of competing interest

The authors declare that they have no known competing financial interests or personal relationships that could have appeared to influence the work reported in this paper.

References

[1] M. Hauser, G. Li, B.J.J.o.N. Nowack, Environmental Hazard Assessment for Polymeric and Inorganic Nanobiomaterials Used in Drug Delivery, vol. 17, 2019.
[2] C. Ferreiro, N. Villota, J.I. Lombraña, M.J. Rivero, An efficient catalytic process for the treatment of genotoxic aniline wastewater using a new granular activated carbon-supported titanium dioxide composite, J. Clean. Prod. 228 (2019) 1282–1295, https://doi.org/10.1016/j.jclepro.2019.04.198.
[3] M.A. Halakarni, A. Samage, A. Mahto, V. Polisetti, S.K. Nataraj, Forward osmosis process for energy materials recovery from industrial wastewater with simultaneous recovery of reusable water: a sustainable approach, Materials Today Sustainability 22 (2023), https://doi.org/10.1016/j.mtsust.2023.100361.
[4] R. Al-Tohamy, S.S. Ali, F. Li, K.M. Okasha, Y.A.G. Mahmoud, T. Elsamahy, H. Jiao, Y. Fu, J. Sun, A critical review on the treatment of dye-containing wastewater: ecotoxicological and health concerns of textile dyes and possible remediation approaches for environmental safety, Ecotoxicol. Environ. Saf. 231 (2022) 113160, https://doi.org/10.1016/j.ecoenv.2021.113160.
[5] J. Iqbal, N.S. Shah, M. Sayed, N.K. Niazi, M. Imran, J.A. Khan, Z.U.H. Khan, A.G.S. Hussien, K. Polychronopoulou, F. Howari, Nano-zerovalent manganese/biochar composite for the adsorptive and oxidative removal of Congo-red dye from aqueous solutions, J. Hazard Mater. 403 (2021) 123854, https://doi.org/10.1016/j.jhazmat.2020.123854.
[6] M. Naushad, A.A. Alqadami, Z.A. AlOthman, I.H. Alsohaimi, M.S. Algamdi, A.M. Aldawsari, Adsorption kinetics, isotherm and reusability studies for the removal of cationic dye from aqueous medium using arginine modified activated carbon, J. Mol. Liq. 293 (2019) 111442, https://doi.org/10.1016/j.molliq.2019.111442.
[7] L. Baloo, M.H. Isa, N.B. Sapari, A.H. Jagaba, L.J. Wei, S. Yavari, R. Razali, R. Vasu, Adsorptive removal of methylene blue and acid orange 10 dyes from aqueous solutions using oil palm wastes-derived activated carbons, Alex. Eng. J. 60 (2021) 5611–5629, https://doi.org/10.1016/j.aej.2021.04.044.
[8] S.U. Jan, A. Ahmad, A.A. Khan, S. Melhi, I. Ahmad, G. Sun, C.M. Chen, R. Ahmad, Removal of azo dye from aqueous solution by a low-cost activated carbon prepared from coal: adsorption kinetics, isotherms study, and DFT simulation, Environ. Sci. Pollut. Res. Int. 28 (2021) 10234–10247, https://doi.org/10.1007/s11356-020-11344-4.
[9] A.M. Chávez, O. Gimeno, A. Rey, G. Pliego, A.L. Oropesa, P.M. Álvarez, F.J. Beltrán, Treatment of highly polluted industrial wastewater by means of sequential aerobic biological oxidation-ozone based AOPs, Chem. Eng. J. 361 (2019) 89–98, https://doi.org/10.1016/j.cej.2018.12.064.

[10] A. Mahto, M.A. Halakarni, A. Maraddi, G. D'Souza, A.A. Samage, U.G. Thummar, D. Mondal, S.K. Nataraj, Upcycling cellulose acetate from discarded cigarette butts: conversion of contaminated microfibers into loose-nanofiltration membranes for selective separation, Desalination 535 (2022), https://doi.org/10.1016/j.desal.2022.115807.

[11] M. Halakarni, A. Mahto, K. Aruchamy, D. Mondal, S.K. Nataraj, Developing helical carbon functionalized chitosan-based loose nanofiltration membranes for selective separation and wastewater treatment, Chem. Eng. J. 417 (2021), https://doi.org/10.1016/j.cej.2020.127911.

[12] A.A. Zewde, L. Zhang, Z. Li, E.A. Odey, A review of the application of sonophotocatalytic process based on advanced oxidation process for degrading organic dye 34 (2019) 365–375, https://doi.org/10.1515/reveh-2019-0024.

[13] H. Yoneyama, Y. Yamashita, H. Tamura, Heterogeneous photocatalytic reduction of dichromate on n-type semiconductor catalysts, Nature 282 (1979) 817–818, https://doi.org/10.1038/282817a0.

[14] S. Boumad, A. Infantes-Molina, I. Barroso-Martín, E. Moretti, E. Rodríguez-Castellón, M.d.C. Román-Martínez, M.Á. Lillo-Ródenas, N. Bouchenafa-Saib, Advantages of the Incorporation of Luffa-Based Activated Carbon to Titania for Improving the Removal of Methylene Blue from Aqueous Solution, vol. 11, 2021, p. 7607.

[15] S. Shen, J. Chen, M. Wang, X. Sheng, X. Chen, X. Feng, S.S. Mao, Titanium dioxide nanostructures for photoelectrochemical applications, Prog. Mater. Sci. 98 (2018) 299–385, https://doi.org/10.1016/j.pmatsci.2018.07.006.

[16] S. Sun, X. Zhang, J. Cui, Q. Yang, S. Liang, Twin engineering of photocatalysts: a minireview, Catal. Sci. Technol. 10 (2020) 4164–4178, https://doi.org/10.1039/d0cy00917b.

[17] L. Yang, D. Fan, Z. Li, Y. Cheng, X. Yang, T.J.A.S.S. Zhang, A Review on the Bioinspired Photocatalysts and Photocatalytic Systems, vol. 6, 2022.

[18] K. Yoshiiri, B. Karabiyik, K. Wang, Z. Wei, C. Colbeau-Justin, E. Kowalska, The property-governed activity of silver-modified titania photocatalysts: the influence of titania matrix, J. Chem. Phys. 156 (2022) 244706, https://doi.org/10.1063/5.0097762.

[19] L. Kong, X. Zuo, S. Zhu, Z. Li, J. Shi, L. Li, Z. Feng, D. Zhang, D. Deng, J. Yu, Novel carbon-poly(silacetylene) composites as advanced thermal protection material in aerospace applications, Compos. Sci. Technol. 162 (2018) 163–169, https://doi.org/10.1016/j.compscitech.2018.04.038.

[20] A. Juno Rose, A. Samage, D. Ghosh, S.K. Nataraj, Preparation of sustainable and binder-free electrode materials for high energy asymmetric supercapacitor applications: a cleaner alternative, J. Clean. Prod. 417 (2023) 137956, https://doi.org/10.1016/j.jclepro.2023.137956.

[21] A. Samage, M. Halakarni, D. Ghosh, S.K. Nataraj, High power, long cycle life capacitive carbon from Hibiscus cannabinus, a Agri-bio-waste withsimultaneous value addition in water treatment application, Chem. Eng. J. 435 (2022) 134952, https://doi.org/10.1016/j.cej.2022.134952.

[22] M.A. Halakarni, A. Samage, A. Mahto, V. Polisetti, S.K. Nataraj, Forward osmosis process for energy materials recovery from industrial wastewater with simultaneous recovery of reusable water: a sustainable approach, Materials Today Sustainability 22 (2023) 100361, https://doi.org/10.1016/j.mtsust.2023.100361.

[23] A. Samage, M. Halakarni, H. Yoon, N. Sanna Kotrappanavar, Sustainable conversion of agricultural biomass waste into electrode materials with enhanced energy density for aqueous zinc-ion hybrid capacitors, Carbon 219 (2024) 118774, https://doi.org/10.1016/j.carbon.2023.118774.

[24] A.R. Singh, P.S. Dhumal, M.A. Bhakare, K.D. Lokhande, M.P. Bondarde, S. Some, In-situ synthesis of metal oxide and polymer decorated activated carbon-based photocatalyst for organic pollutants degradation, Separ. Purif. Technol. 286 (2022) 120380, https://doi.org/10.1016/j.seppur.2021.120380.

[25] M. Gayathiri, T. Pulingam, K.T. Lee, K. Sudesh, Activated carbon from biomass waste precursors: factors affecting production and adsorption mechanism, Chemosphere 294 (2022) 133764, https://doi.org/10.1016/j.chemosphere.2022.133764.

[26] C. Parvathiraja, S. Katheria, M.R. Siddiqui, S.M. Wabaidur, M.A. Islam, W.-C. Lai, Activated Carbon-Loaded Titanium Dioxide Nanoparticles and Their Photocatalytic and Antibacterial Investigations, vol. 12, 2022, p. 834.

[27] Z. Cai, X. Deng, Q. Wang, J. Lai, H. Xie, Y. Chen, B. Huang, G. Lin, Core-shell granular activated carbon and its adsorption of trypan blue, J. Clean. Prod. 242 (2020) 118496, https://doi.org/10.1016/j.jclepro.2019.118496.

[28] K. Kierzek, G. Gryglewicz, Activated Carbons and Their Evaluation in Electric Double Layer Capacitors, vol. 25, 2020, p. 4255.

[29] E. Ortiz-Ortega, S. Hosseini, S.O. Martinez-Chapa, M.J. Madou, Aging of plasma-activated carbon surfaces: challenges and opportunities, Appl. Surf. Sci. 565 (2021) 150362, https://doi.org/10.1016/j.apsusc.2021.150362.

[30] I. Lansari, B. Benguella, N. Kruchinina, A. Nistratov, Adsorption of textile dyes from aqueous solution using activated carbon from human hair, React. Kinet. Mech. Catal. 135 (2022) 1891–1903, https://doi.org/10.1007/s11144-022-02224-8.

[31] K. Durairaj, P. Senthilkumar, P. Velmurugan, S. Divyabharathi, D. Kavitha, Development of activated carbon fromNerium oleanderflower and their rapid adsorption of direct and reactive dyes, Int. J. Green Energy 16 (2019) 573–582, https://doi.org/10.1080/15435075.2019.1598419.

[32] Y. Yue, Z. Yu, X. Yue, W. Zhou, S. Wang, Y. Yang, Y. Lao, M. Yang, C. Du, S. Wang, Activated carbon derived from highland barley straw for removing heavy metals and organic pollutants, Int. J. Low Carbon Technol. 19 (2023) 135–141, https://doi.org/10.1093/ijlct/ctad042. %J International Journal of Low-Carbon Technologies.

[33] G. Feng, F. Jiang, Z. Hu, W. Jiang, J. Liu, Q. Zhang, Q. Wu, Q. Hu, L. Miao, S. Cheng, A novel porous egg-white (EW)/titania composite photocatalytic material for efficient photodegradation applications, RSC Adv. 10 (2020) 8525, https://doi.org/10.1039/d0ra00730g.

[34] A. Kundu, A. Mondal, Kinetics, isotherm, and thermodynamic studies of methylene blue selective adsorption and photocatalysis of malachite green from aqueous solution using layered Na-intercalated Cu-doped Titania, Appl. Clay Sci. 183 (2019) 105323, https://doi.org/10.1016/j.clay.2019.105323.

[35] A. Fattahi, R. Liang, A. Kaur, O. Schneider, M.J. Arlos, P. Peng, M. Servos, N. Zhou, Photocatalytic degradation using TiO2-graphene nanocomposite under UV-LED illumination: optimization using response surface methodology, J. Environ. Chem. Eng. 7 (2019), https://doi.org/10.1016/j.jece.2019.103366.

[36] R. Chen, N. Han, L. Li, S. Wang, X. Ma, C. Wang, H. Li, H. Li, L. Zeng, Fundamental understanding of oxygen content in activated carbon on acetone adsorption desorption, Appl. Surf. Sci. 508 (2020) 145211, https://doi.org/10.1016/j.apsusc.2019.145211.

[37] H. Zhang, The size dependence of the surface free energy of titania nanocrystalsElectronic supplementary information (ESI) available: XRD data, TEM images (2000), https://doi.org/10.1039/b819623k. See.

[38] Y. Yang, A. Hong, Y. Liang, K. Xu, T. Yu, J. Shi, F. Zeng, Y. Qu, Y. Liu, M. Ding, et al., High-energy {001} crystal facets and surface fluorination engineered gas sensing properties of anatase titania nanocrystals, Appl. Surf. Sci. 423 (2017) 602–610, https://doi.org/10.1016/j.apsusc.2017.06.208.

[39] P.S. Das, S. Bakuli, I. Biswas, A.K. Mallik, A. Dey, S. Mukherjee, J. Ghosh, A.K. Mukhopadhyay, RGO/MgO hybrid nanocomposites with high specific capacitance, Ceram. Int. 44 (2018) 424–432, https://doi.org/10.1016/j.ceramint.2017.09.194.

[40] Y. Chen, H. Zhao, Y. Ning, B. Zhao, J. Zheng, T. Yang, M. Liu, F. Yin, S. Li, L.J.R.A. Chen, Spontaneous Growth of Silver Nanotrees Dominated with (111) Crystalline Faces on Monolithic Activated Carbon, vol. 6, 2016.

[41] S. Bourahla, F. Nemchi, H. Belayachi, A. Belayachi, C. Harrats, M. Belhakem, Removal of the AO7 dye by adsorption on activated carbon based on grape marc: equilibrium, regeneration, and FTIR spectroscopy, J. Iran. Chem. Soc. 20 (2023) 669–681, https://doi.org/10.1007/s13738-022-02705-6.

[42] J. Wang, T.-L. Liu, Q.-X. Huang, Z.-Y. Ma, Y. Chi, J.-H. Yan, Production and characterization of high quality activated carbon from oily sludge, Fuel Process. Technol. 162 (2017) 13–19, https://doi.org/10.1016/j.fuproc.2017.03.017.

[43] J. Raskó, T. Bánsági, F. Solymosi, HCN adsorption on silica and titania supported Rh catalysts studied by FTIR 4 (2002) 3509–3513.

[44] E.M. El Mouchtari, C. Daou, S. Rafqah, F. Najjar, H. Anane, A. Piram, A. Hamade, S. Briche, P. Wong-Wah-Chung, TiO2 and activated carbon of Argania Spinosa tree nutshells composites for the adsorption photocatalysis removal of pharmaceuticals from aqueous solution, J. Photochem. Photobiol. Chem. 388 (2020) 112183, https://doi.org/10.1016/j.jphotochem.2019.112183.

[45] H. Wang, H. Guo, Y. Liu, C. Yi, J. Chu, Regeneration of activated carbon spent with phenol and formation of hydrogen peroxide in a pulsed discharge plasma system, IEEE Trans. Plasma Sci. 44 (2016) 1834–1841, https://doi.org/10.1109/TPS.2016.2593708.

[46] R. Al-Gaashani, D. Almasri, B. Shomar, V. Kochkodan, Preparation and properties of novel activated carbon doped with aluminum oxide and silver for water treatment, J. Alloys Compd. 858 (2021) 158372, https://doi.org/10.1016/j.jallcom.2020.158372.

[47] K. Elizaveta, M. Anton, B. Artemii, I. Vladimir, S.A. James, B. Olga, Unveiling Point Defects in Titania Mesocrystals: a Combined EPR and XPS Study, 2018, 10.1039.C1038NJ03196G-.

[48] D.T.N. Hoa, N.T.T. Tu, H.Q.A. Thinh, L. Van Thanh Son, L.V.T. Son, N.D.V. Quyen, L.L. Son, T.N. Tuyen, P.L.M. Thong, L.H. Diem, et al., TiO2/g-C3N4 visible-light-driven photocatalyst for methylene blue decomposition, J. Nanomater. 2023 (2023) 1–15, https://doi.org/10.1155/2023/9967890.
[49] H. Shi, Y. Chen, J. Lu, H. Guo, H. Qiu, P. Li, Visible light photocatalytic degradation of methylene blue by hydrated titanium dioxide nanoparticles incorporated within rice straw, Appl. Nanosci. 11 (2021) 921–931, https://doi.org/10.1007/s13204-020-01656-9.
[50] L.T.T. Tuyen, D.A. Quang, T.T. Tam Toan, T.Q. Tung, T.T. Hoa, T.X. Mau, D.Q. Khieu, Synthesis of CeO2/TiO2 nanotubes and heterogeneous photocatalytic degradation of methylene blue, J. Environ. Chem. Eng. 6 (2018) 5999–6011, https://doi.org/10.1016/j.jece.2018.09.022.
[51] S. Anita, T.A. Hanifah, G.F. Kartika, P.H. Yanti, Methylene blue and methyl orange dyes removal using low-cost composite of banana peel-TiO2 adsorbent, J. Phys. Conf. 1819 (2021), https://doi.org/10.1088/1742-6596/1819/1/012060.
[52] H. Bayahia, Green synthesis of activated carbon doped tungsten trioxide photocatalysts using leaf of basil (Ocimum basilicum) for photocatalytic degradation of methylene blue under sunlight, J. Saudi Chem. Soc. 26 (2022) 101432, https://doi.org/10.1016/j.jscs.2022.101432.